Regulating surface potential maximizes voltage in all-perovskite tandems

https://doi.org/10.1038/s41586-022-05541-z

Received: 24 June 2022

Accepted: 8 November 2022

Published online: 15 November 2022

Check for updates

Hao Chen[1,8], Aidan Maxwell[1,8], Chongwen Li[1,2,8], Sam Teale[1,8], Bin Chen[1,3,8], Tong Zhu[1], Esma Ugur[4], George Harrison[4], Luke Grater[1], Junke Wang[1], Zaiwei Wang[1], Lewei Zeng[1], So Min Park[1], Lei Chen[2], Peter Serles[5], Rasha Abbas Awni[2], Biwas Subedi[2], Xiaopeng Zheng[6], Chuanxiao Xiao[6], Nikolas J. Podraza[2], Tobin Filleter[5], Cheng Liu[3,7], Yi Yang[3,7], Joseph M. Luther[6], Stefaan De Wolf[4], Mercouri G. Kanatzidis[3], Yanfa Yan[2]✉ & Edward H. Sargent[1,3,7]✉

The open-circuit voltage (V_{OC}) deficit in perovskite solar cells is greater in wide-bandgap (over 1.7 eV) cells than in perovskites of roughly 1.5 eV (refs. [1,2]). Quasi-Fermi-level-splitting measurements show V_{OC}-limiting recombination at the electron-transport-layer contact[3–5]. This, we find, stems from inhomogeneous surface potential and poor perovskite–electron transport layer energetic alignment. Common monoammonium surface treatments fail to address this; as an alternative, we introduce diammonium molecules to modify perovskite surface states and achieve a more uniform spatial distribution of surface potential. Using 1,3-propane diammonium, quasi-Fermi-level splitting increases by 90 meV, enabling 1.79 eV perovskite solar cells with a certified 1.33 V V_{OC} and over 19% power conversion efficiency (PCE). Incorporating this layer into a monolithic all-perovskite tandem, we report a record V_{OC} of 2.19 V (89% of the detailed balance V_{OC} limit) and over 27% PCE (26.3% certified quasi-steady state). These tandems retained more than 86% of their initial PCE after 500 h of operation.

The wide range of bandgaps achievable using metal-halide perovskites (around 1.2–3.0 eV) has enabled the development of tandem solar cells with silicon, copper indium gallium selenide and organic photovoltaics[6–9]. Recently, all-perovskite tandems made from stacked wide-bandgap (WBG; approximately 1.8 eV) and narrow-bandgap (NBG; approximately 1.2 eV) layers surpassed the highest recorded power conversion efficiency (PCE) for a single-junction perovskite solar cell (PSC)[10,11].

Despite rapid progress, the PCE of perovskite tandems is limited by the large open-circuit voltage (V_{OC}) loss of the WBG cell[1,2]. Whereas single-junction PSCs of around 1.5 eV have demonstrated V_{OC} deficits (the difference between the bandgap and device V_{OC}) as low as 0.3 V[12], mixed iodide/bromide PSCs over 1.75 eV have yet to achieve V_{OC} deficits lower than 0.5 V (Supplementary Fig. 1)[13,14]. The V_{OC} deficit has been suggested to stem from increased trap density in perovskites with over 20% Br concentration, photoinduced halide segregation and poor energetic alignment with charge transport layers[15,16]. The photoluminescence quantum yield (PLQY) of perovskites, once in contact with charge transport layers, tends to decrease markedly, suggesting that the perovskite–transport layer interface produces recombination pathways within the perovskite bandgap[3–5]. Several causes have been reported in efforts to uncover the origin of this phenomenon, including band misalignment[16], energy-level pinning[5] and halide migration from the perovskite into the transport layer[17]. Here we examine the perovskite–C_{60} interface because it is ubiquitous in perovskite tandems, is the most easily accessed interface when fabricating inverted (*pin*) PSCs and yet is still considered one of the worst offenders in regard to induction of trap states[5,16].

We spin-coated WBG perovskite ($Cs_{0.2}FA_{0.8}Pb(I_{0.6}Br_{0.4})_3$) films on top of indium tin oxide (ITO)/hole transport layer (HTL) substrates with the structure ITO/NiOx/[4-(3,6-dimethyl-9H-carbazol-9-yl)butyl] phosphonic acid (Me-4PACz) and measured their PLQY with and without a C_{60} layer (Fig. 1b). Consistent with previous reports[3,5] we found that, after C_{60} deposition, the PLQY is two orders of magnitude lower, equivalent to a drop of about 100 meV in quasi-Fermi-level splitting (QFLS)[18].

Previous studies have focused on post treatments that reduce the defect density of the perovskite surface and thus increase the PLQY of films[19–22]. Extending this practice to WBG perovskites, we found that treating the surface with the popular passivant butylammonium iodide (BA) increases PLQY but that the improvement was not retained following deposition of C_{60} (Fig. 1b). Indeed, the QFLS of the stack is probably pinned due to interfacial recombination rather than the inherent trap density of the perovskite[5].

Seeking a different approach, we reasoned that tuning the surface potential at the perovskite–C_{60} interface would suppress this cross-interface recombination by reducing band offset between perovskite and C_{60}, and by reducing the population of minority carriers at the interface. This effect is analogous to field-effect passivation in traditional Si solar cells[23,24]. Thus, we turned our focus toward short-chain

[1]The Edward S. Rogers Department of Electrical and Computer Engineering, University of Toronto, Toronto, Ontario, Canada. [2]Department of Physics and Astronomy and Wright Center for Photovoltaics Innovation and Commercialization, The University of Toledo, Toledo, OH, USA. [3]Department of Chemistry, Northwestern University, Evanston, IL, USA. [4]KAUST Solar Center, Physical Sciences and Engineering Division, King Abdullah University of Science and Technology, Thuwal, Kingdom of Saudi Arabia. [5]Department of Mechanical and Industrial Engineering, University of Toronto, Toronto, Ontario, Canada. [6]National Renewable Energy Laboratory, Golden, CO, USA. [7]Department of Electrical and Computer Engineering, Northwestern University, Evanston, IL, USA. [8]These authors contributed equally: Hao Chen, Aidan Maxwell, Chongwen Li, Sam Teale, Bin Chen. ✉e-mail: yanfa.yan@utoledo.edu; ted.sargent@utoronto.ca

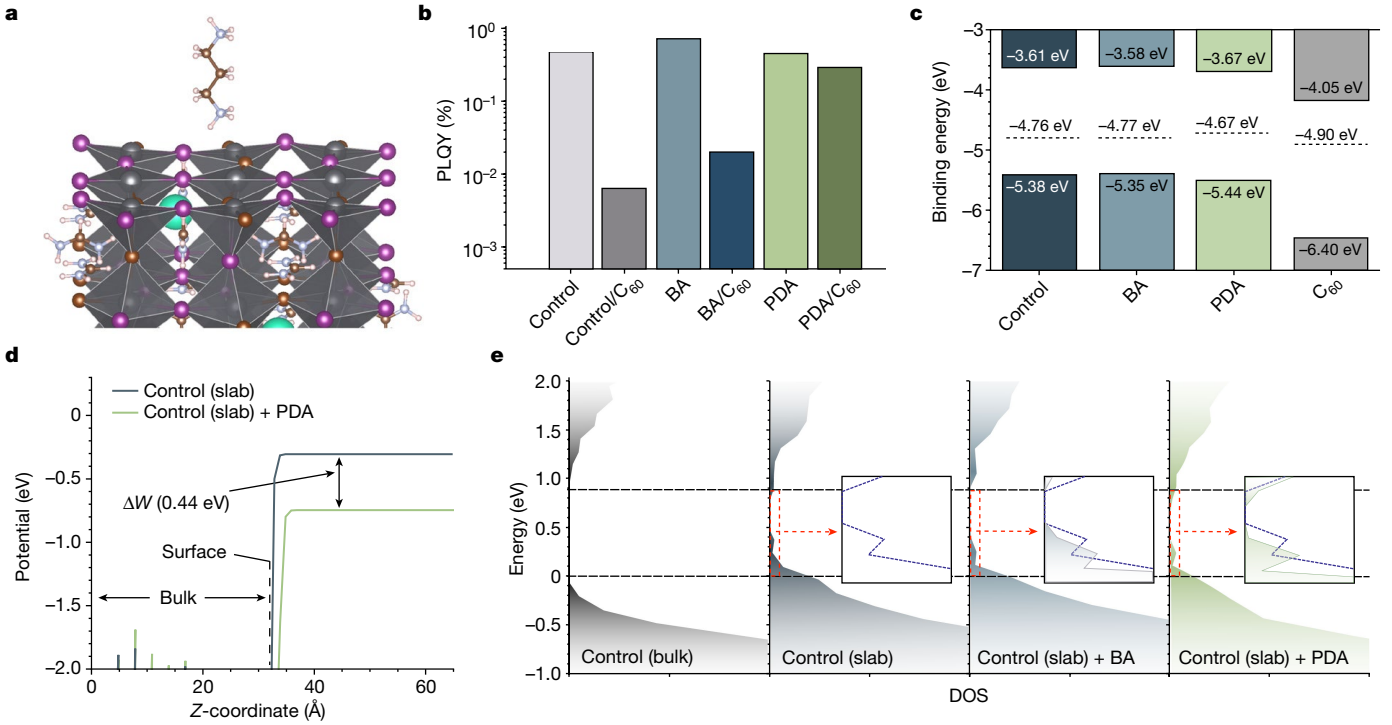

Fig. 1 | Analysis and strategies for the minimization of recombination between perovskite and ETL. a, Schematic crystal structure of perovskite surface treated with a PDA ligand. **b**, PLQY data from control, BA- and PDA-treated films, with and without C_{60}, on an ITO/HTL substrate. **c**, Band alignment of control and BA- and PDA-treated films compared with C_{60} (values from UPS/inverse photoelectron spectroscopy (IPES) measurements in Supplementary Fig. 2). Binding energy plotted with respect to vacuum level E_{Vac}. **d**, Work function difference (ΔW) between an untreated and PDA-treated Pb-I-terminated surface with a bromide vacancy (V_{Br}), obtained by calculation of electrostatic potential difference: $\Delta W = \Delta P = P_{untreated} - P_{treated}$. As a result, positive and negative values for ΔW represent Fermi-level upshift and downshift, respectively. **e**, DOS calculated for bulk perovskite and different surface structures. Detailed DOS plots in the gap region are shown in zoomed-in insets, in which the control (slab) DOS are represented by blue dashed lines.

diammonium ligands, strong Lewis bases previously shown to induce n-type doping and surface dipoles that alter surface energetics in mixed Pb–Sn perovskites[25–27]. Treating the perovskite surface with 1,3-propane-diammonium iodide (PDA) (Fig. 1a), the diammonium equivalent to BA, we observed only a slight increase in PLQY. However, following deposition of C_{60} there was no marked drop in PLQY, suggesting that the recombination pathways induced by C_{60} had been effectively suppressed. We also compared the effects of perovskite post treatments with similar concentrations of 1,2-ethane-diammonium iodide (EDA) and 1,4-butane-diammonium iodide, diammonium ligands with a shorter and longer chain length, respectively. Of these diammonium ligands, only PDA resulted in retention of PLQY after deposition of C_{60} (Supplementary Fig. 3).

To understand how both treatments affect interface energetics, we used ultraviolet photoelectron spectroscopy (UPS) and found that BA induces a Fermi-level downshift whereas PDA induces a Fermi-level upshift, resulting in stronger and weaker surface p-type doping, respectively (Fig. 1c). The latter change in surface potential produces a lower minority carrier concentration at the interface and reduces band offset between perovskite and C_{60} by 60 meV. Drift-diffusion modelling suggests that this has the potential to increase QFLS by approximately 90 meV (Supplementary Fig. 4).

Using time-of-flight secondary ion mass spectrometry and X-ray photoelectron spectroscopy (Supplementary Figs. 5 and 6), we found that PDA ligands are present on the film surface after treatment. Using density functional theory, we studied work function changes following PDA treatment of various surface structures (Supplementary Fig. 7 and Fig. 1d). Among considered surface configurations, the pristine Pb-I-terminated surface with a bromide vacancy (V_{Br}), which exhibited a lower work function (by 0.44 eV) after PDA treatment (Supplementary Fig. 8), was in best agreement with the 0.1 eV shift obtained from experimental UPS data. Then, through density of states (DOS) analysis of BA and PDA surface treatments (Fig. 1e and Supplementary Fig. 9) we found that, after PDA treatment, the in-gap surface states near the valence band maximum region were suppressed (Supplementary Materials), consistent with Fermi-level upshift relative to the valence band maximum (Fig. 1c) observed in UPS measurements.

Seeking to investigate how PDA affects films at the nanoscale, we used hyperspectral imaging to generate QFLS maps of perovskite films with and without C_{60} (Fig. 2a,b and Supplementary Fig. 10). From these maps we observed significantly greater spatial fluctuation than that observed for perovskites with narrower bandgaps (under 1.65 eV), which have a typical standard deviation (σ) in QFLS of around 10 meV[4,28]. After PDA treatment, however, σ was lowered significantly (from 61 to 24 meV), suggesting that the treated film is more homogeneous. After C_{60} deposition the QFLS of the control dropped (1.32 to 1.25 eV) and broadened further (σ = 77 meV), whereas that of the PDA film was maintained at 1.33 eV but with a slightly narrower distribution (σ = 22 meV). Kelvin probe force microscopy (KPFM) (Fig. 2c,d and Supplementary Fig. 11) suggested that this effect is correlated with the nonuniform contact potential of the control film, which will act to broaden interfacial electronic states when in contact with C_{60} leading to increased recombination[5,29]. PDA treatment narrowed contact potential distribution significantly (σ = 2.9 mV compared with 11.1 mV for the control), which is indicative of reduced recombination and improved carrier extraction[30,31].

We used grazing incidence wide-angle X-ray scattering (GIWAXS) to show the crystallographic consequences of PDA treatment. Varying the incident angle of the X-ray beam, we compared the crystal structure of the film bulk (1.00°) and surface (0.15°) (Fig. 2e–h and Supplementary Fig. 12). In contrast to previous perovskite systems

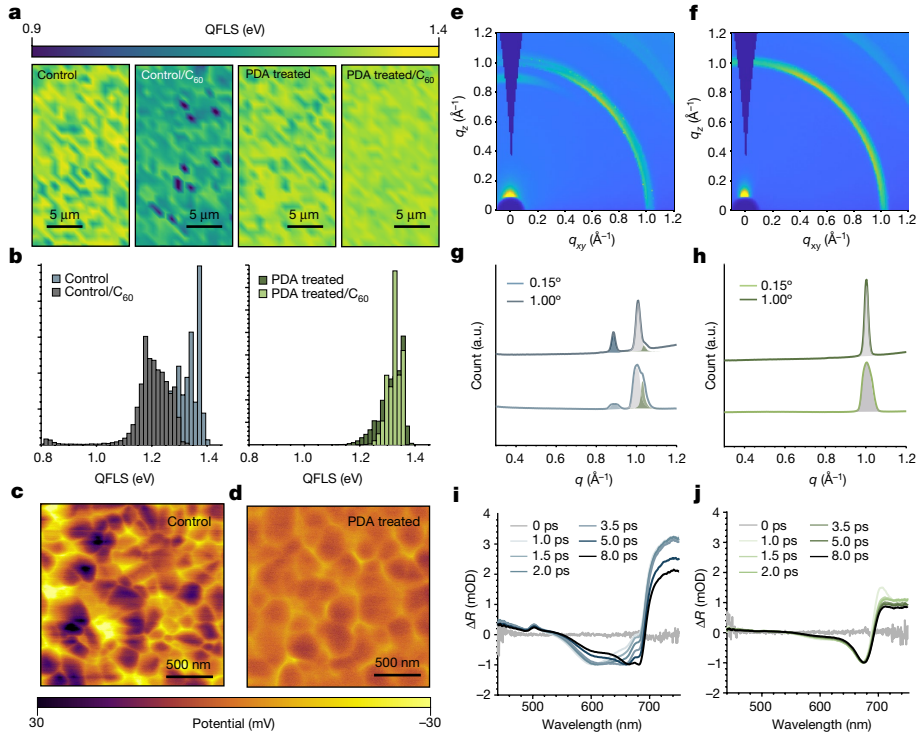

Fig. 2 | Surface inhomogeneity and its remediation using surface-adsorbed molecular layers. a, QFLS maps of control and PDA-treated films demonstrating increased homogeneity and resistance to C_{60}-induced defects. **b**, Histograms of QFLS pixel values taken from larger (100 × 100 μm²) images (Supplementary Fig. 10). **c**,**d**, KPFM images of control (**c**) and PDA-treated (**d**) films. **e**,**f**, GIWAXS patterns of control (**e**) and PDA-treated (**f**) films at 0.15° incident angle. **g**,**h**, Azimuthal integrations comparing surface (0.15°) and bulk (1.00°) crystal structures for control (**g**) and PDA-treated (**h**) films. **i**,**j**, Transient reflection measurements of control (**i**) and treated (**j**) films showing the transient reflectivity change (measured in optical density) over a timescale of 8.0 ps. Films were encapsulated between two glass slides to mitigate environmental damage.

treated with diammonium ligands, there exist no low-q-value peaks for the PDA-treated film and, thus, no indication of reduced-dimensional perovskite formation[32,33], nor of a perovskite polymorph[34]. The concentration of PDA spin-coated onto the perovskite surface is low and thus does not appear to result in appreciable diffusion into the bulk perovskite. Two structural differences between control and treated

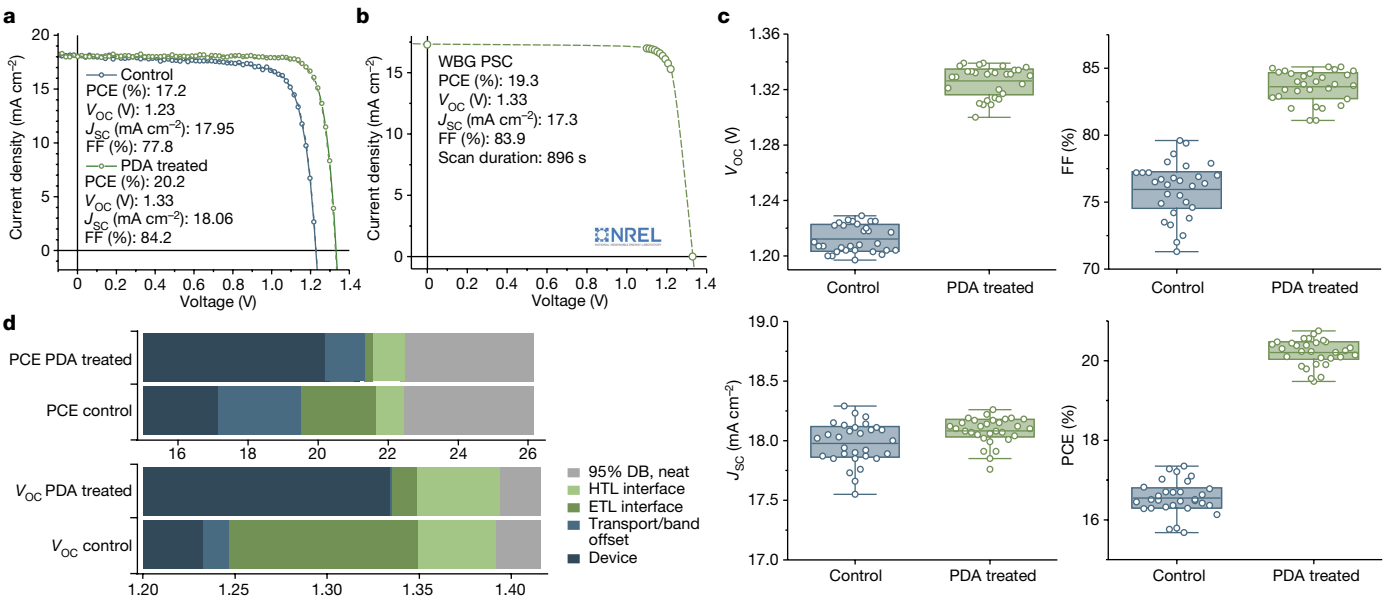

Fig. 3 | Characterization of WBG perovskite solar cells. a, J–V curves of control and PDA-treated WBG devices. **b**, NREL-certified J–V curve of PDA-treated WBG perovskite solar cell. Devices were encapsulated to mitigate environmental damage. **c**, PV parameters of control and treated devices (30 devices for each type). **d**, Loss analysis for PCE and V_{OC} of control and treated devices. PCE and V_{OC} losses were extracted from pseudo-J–V measurements shown in Supplementary Fig. 18 and Supplementary Table 3. 95% DB represents 95% of the detailed balance limit for V_{OC}, and corresponding PCE.

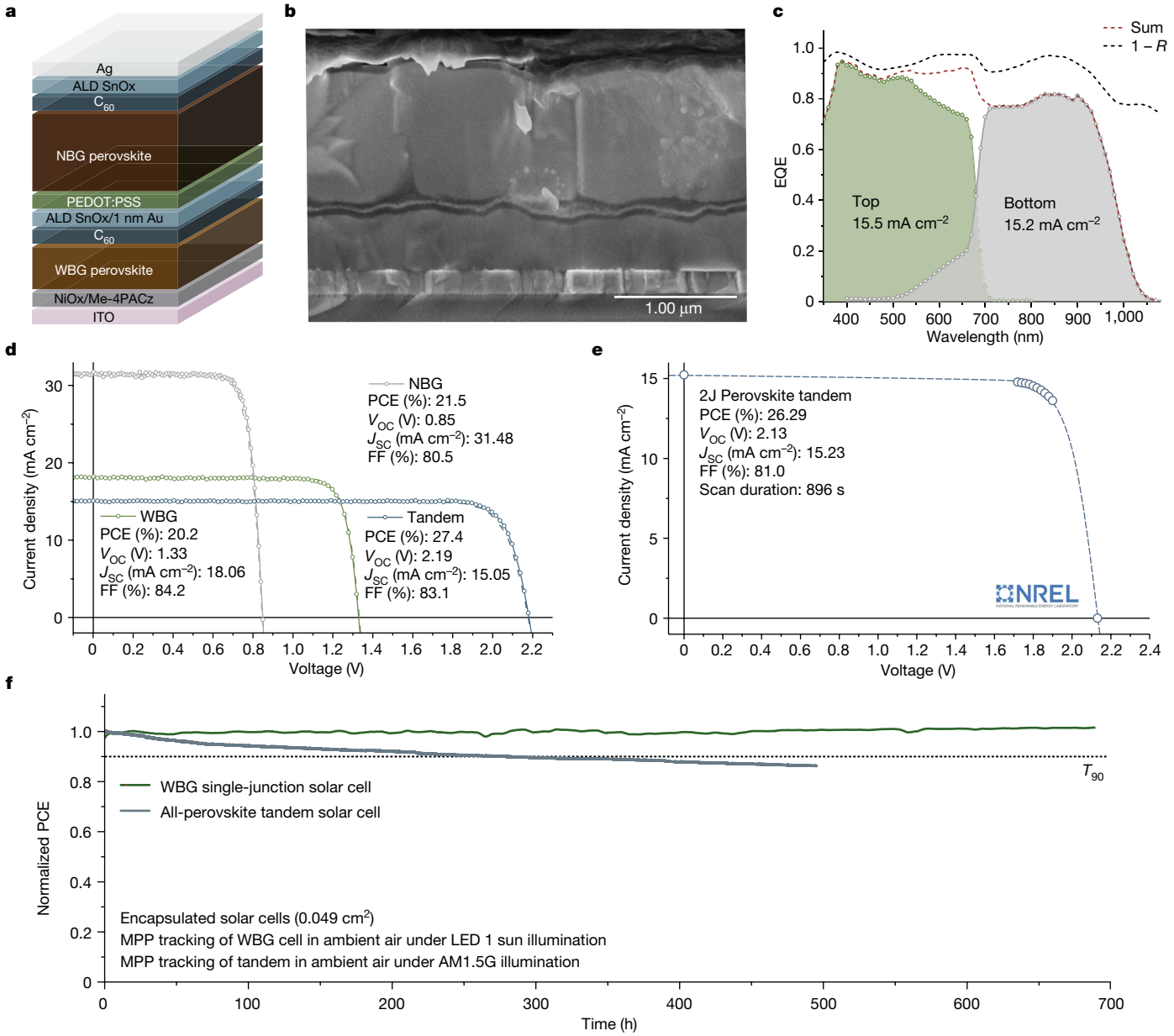

Fig. 4 | PV performance and stability of perovskite tandem solar cells. **a**, Schematic diagram of tandem device structure. **b**, Cross-sectional SEM image of tandem device. **c**, EQE curves of WBG and NBG subcells within the tandem device, showing losses due to reflectance ($1-R$). **d**, J–V curves of champion NBG, WBG and all-perovskite tandem devices. **e**, NREL-certified J–V curve of all-perovskite tandem device (Supplementary Fig. 23). **f**, MPP stability tracking of encapsulated WBG and tandem devices under ambient conditions with simulated 1 sun illumination (initial PCE of 19.0% and 26.9%, respectively). T_{90} represents the time taken for the device efficiency to drop to 90% of its original value. The tandem device retained over 86% of initial efficiency after 500 h of operation.

films are apparent, however: (1) a peak at 0.88 $Å^{-1}$ for the control that we ascribe to PbI_2, which was entirely removed by PDA, and (2) a secondary peak with a q-space value of 1.03 $Å^{-1}$ alongside the (1 1 0) perovskite peak (1.00 $Å^{-1}$), indicative of a Br-rich phase. This secondary peak is more obvious when probing only the first 5 nm or so of film, suggesting that the film surface is segregated into PbI_2- and Br-rich perovskite regions, the probable cause of the broad contact potential[35]. The suppression of surface phase segregation and removal of PbI_2 implies that, whereas PDA does not induce the formation of a new crystal phase, it does react with the surface of the perovskite. This has been observed previously with diammoniums that template the growth of perovskite crystallization[36,37], and is corroborated by scanning electron microscopy (SEM) images (Supplementary Fig. 13), transient absorption (Supplementary Fig. 14) and transient reflection spectra (Fig. 2i,j). Transient reflection spectra show that two additional bleaches are present in the control compared with the PDA-treated sample: a peak around 500 nm (PbI_2) and a fast-decaying bleach at around 600 nm (approximately 85% Br-rich perovskite, which correlates exactly with the shift in q-space seen in GIWAXS)[38].

Encouraged by the reduced interfacial recombination and surface homogeneity imparted by PDA treatment, we fabricated WBG solar cells. The device structure was ITO/NiOx/Me-4PACz/perovskite/C_{60}/ALD SnOx/Ag, in which Me-4PACz is a self-assembled monolayer of [4-(3,6-dimethyl-9H-carbazol-9-yl)butyl]phosphonic acid. Figure 3a shows the forward and reverse J–V curves for champion control and PDA-treated 1.79 eV WBG PSCs (external quantum efficiency (EQE) spectrum shown in Supplementary Fig. 15), exhibiting an increase in V_{OC} from 1.23 to 1.33 V, the highest value of V_{OC} reported for PSCs of

around 1.8 eV (Supplementary Fig. 1). Figure 3b shows the *J*–*V* curve of a PDA-treated PSC exhibiting a V_{OC} of around 1.33 V and PCE of 19.3%, as verified by the photovoltaic (PV) cell and module performance group at the National Renewable Energy Lab (NREL) (Supplementary Fig. 16). Improvements in device V_{OC}, fill factor (FF) and PCE were consistent across 30 control and PDA-treated devices, as shown in Fig. 3c. We also fabricated 1 cm^2 WBG devices using PDA surface treatment, which delivered a V_{OC} of around 1.35 V and PCE of 19.0% (Supplementary Fig. 17).

We conducted transient photovoltage and photocurrent measurements of control and PDA-treated devices (Supplementary Fig. 19). The charge-recombination lifetime (τ_r) of the PDA-treated device was longer than that of the control device (2.0 µs compared to 0.4 µs), consistent with reduced carrier trapping at the C_{60} interface after PDA post treatment (Supplementary Fig. 20 and Supplementary Table 4)[39]. Calculating diffusion length (Supplementary Note 2), we found that PDA treatment resulted in a twofold increase, from 600 nm to 1.2 µm.

We followed the output of a PDA-treated WBG cell operating for 700 h at the maximum power point (MPP) to determine the impact of PDA on device stability (Supplementary Fig. 21). After 700 h of continuous operation under 1 sun illumination, the PDA-treated device exhibited no loss in PCE. We attribute this to an increased ion migration barrier exhibited in PDA-treated films, calculated from thermal admittance spectroscopy (Supplementary Fig. 22).

We used intensity-dependent PLQY measurements to conduct systematic loss analysis (pseudo-*J*–*V*) of control versus PDA-treated films (Fig. 3d and Supplementary Table 3)[40]. Both samples have similar bulk and HTL interface losses, but PDA treatment reduced V_{OC} loss at the electron transport layer (ETL) from 104 to 16 mV. PDA also eliminated a 14 mV mismatch between the full-stack QFLS and device V_{OC} present in the control sample, indicating a reduced band offset between perovskite and C_{60} after treatment[16], consistent with the band alignment analysis shown in Fig. 1. In addition to reduced V_{OC} loss, PDA-treated devices exhibited reduced transport (FF) losses compared with the control (3.4%$_{abs.}$ versus 8.0%$_{abs.}$) (Supplementary Table 3). This also suggests favourable band bending at the treated interface, resulting in improved carrier extraction.

Using our high-V_{OC} PDA-treated WBG active layer in combination with a $Cs_{0.05}FA_{0.7}MA_{0.25}Pb_{0.5}Sn_{0.5}I_3$ NBG mixed Pb–Sn perovskite (approximately 1.2 eV), we fabricated monolithic all-perovskite tandem solar cells (Methods). The tandem device structure was ITO/NiOx/Me-4PACz/WBG perovskite/C_{60}/ALD SnOx/Au (1 nm)/poly(3,4-ethylenedioxythiophene) polystyrene sulfonate (PEDOT:PSS)/NBG perovskite/C_{60}/ALD SnOx/Ag (Fig. 4a); the SEM cross-sectional image shows the thick Pb–Sn perovskite layer (approximate thickness 1.0 µm) needed for current matching (Fig. 4b)[10]. The integrated short-circuit current density (J_{SC}) values for WBG and NBG subcells from EQE measurements of a tandem device were 15.4 and 15.2 mA cm^{-2}, respectively (Fig. 4c). Bandgaps of WBG and NBG subcells calculated from the EQE spectra were 1.79 and 1.22 eV, respectively.

Figure 4d shows forward and reverse *J*–*V* scans of a champion tandem, WBG and NBG PSCs. A record PCE of 27.4% was achieved with a high V_{OC} of 2.19 V, along with a J_{SC} of 15.1 mA cm^{-2} and FF of 83.1%. The 2.19 V V_{OC} represents a significant improvement over the previous highest reported V_{OC} among the best all-perovskite tandems[10,41–44] because of the high V_{OC} of the PDA-treated WBG subcell. We sent a tandem cell to an accredited independent PV calibration laboratory (NREL). The device delivered a certified PCE of 26.29% and V_{OC} of 2.13 V (Fig. 4e and Supplementary Fig. 23), representing a certified all-perovskite tandem that surpasses the record PCE (25.7%) of single-junction perovskite solar cells using the asymptotic maximum power (P_{max}) scan protocol[11,45]. We also fabricated 1 cm^2 all-perovskite tandem solar cells, which delivered a PCE of 26.03% and V_{OC} of 2.16 V (Supplementary Fig. 24). We note that there is still room for improvement, particularly in the J_{SC} value of the tandem because J_{SC} values of over 16.5 mA cm^{-2} have been reported[10]. Therefore, we anticipate that PCEs approaching 30% are already experimentally feasible.

We tested operating stability using MPP tracking of an encapsulated tandem in ambient air (Fig. 4f). Under global standard spectrum (AM1.5G) 1 sun illumination at MPP, the device retained 86% of its initial PCE after 500 h of continuous operation. This promising operating stability, in combination with high V_{OC} and PCE enabled by diammonium surface modification, represents an important step towards the application of all-perovskite tandem solar cells.

Online content

Any methods, additional references, Nature Portfolio reporting summaries, source data, extended data, supplementary information, acknowledgements, peer review information; details of author contributions and competing interests; and statements of data and code availability are available at https://doi.org/10.1038/s41586-022-05541-z.

1. Oliver, R. D. J. et al. Understanding and suppressing non-radiative losses in methylammonium-free wide-bandgap perovskite solar cells. *Energy Environ. Sci.* **15**, 714–726 (2022).
2. Mahesh, S. et al. Revealing the origin of voltage loss in mixed-halide perovskite solar cells. *Energy Environ. Sci.* **13**, 258–267 (2020).
3. Stranks, S. D., Hoye, R. L. Z., Di, D., Friend, R. H. & Deschler, F. The physics of light emission in halide perovskite devices. *Adv. Mater.* **31**, 1803336 (2019).
4. Stolterfoht, M. et al. Visualization and suppression of interfacial recombination for high-efficiency large-area pin perovskite solar cells. *Nat. Energy* **3**, 847–854 (2018).
5. Warby, J. et al. Understanding performance limiting interfacial recombination in pin perovskite solar cells. *Adv. Energy Mater.* **12**, 2103567 (2022).
6. Wang, R. et al. Prospects for metal halide perovskite-based tandem solar cells. *Nat. Photon.* **15**, 411–425 (2021).
7. Leijtens, T., Bush, K. A., Prasanna, R. & McGehee, M. D. Opportunities and challenges for tandem solar cells using metal halide perovskite semiconductors. *Nat. Energy* **3**, 828–838 (2018).
8. Al-Ashouri, A. et al. Monolithic perovskite/silicon tandem solar cell with >29% efficiency by enhanced hole extraction. *Science* **370**, 1300–1309 (2020).
9. Chen, W. et al. Monolithic perovskite/organic tandem solar cells with 23.6% efficiency enabled by reduced voltage losses and optimized interconnecting layer. *Nat. Energy* **7**, 229–237 (2022).
10. Lin, R. et al. All-perovskite tandem solar cells with improved grain surface passivation. *Nature* **603**, 73–78 (2022).
11. NREL. Best research-cell efficiency chart. https://www.nrel.gov/pv/cell-efficiency.html (accessed 21 November 2022).
12. Jeong, M. et al. Stable perovskite solar cells with efficiency exceeding 24.8% and 0.3-V voltage loss. *Science* **369**, 1615–1620 (2020).
13. Zhang, J. et al. Intermediate phase enhances inorganic perovskite and metal oxide interface for efficient photovoltaics. *Joule* **4**, 222–234 (2020).
14. Liu, Z., Siekmann, J., Klingebiel, B., Rau, U. & Kirchartz, T. Interface optimization via fullerene blends enables open-circuit voltages of 1.35 V in $CH_3NH_3Pb(I_{0.8}Br_{0.2})_3$ solar cells. *Adv. Energy Mater.* **11**, 2003386 (2021).
15. Tong, J. et al. Wide-bandgap metal halide perovskites for tandem solar cells. *ACS Energy Lett.* **6**, 232–248 (2021).
16. Stolterfoht, M. et al. The impact of energy alignment and interfacial recombination on the internal and external open-circuit voltage of perovskite solar cells. *Energy Environ. Sci.* **12**, 2778–2788 (2019).
17. Zhao, T., Chueh, C. C., Chen, Q., Rajagopal, A. & Jen, A. K. Y. Defect passivation of organic-inorganic hybrid perovskites by diammonium iodide toward high-performance photovoltaic devices. *ACS Energy Lett.* **1**, 757–763 (2016).
18. Ross, R. T. Some thermodynamics of photochemical systems. *J. Chem. Phys.* **46**, 4590 (2004).
19. Teale, S. et al. Dimensional mixing increases the efficiency of 2D/3D perovskite solar cells. *J. Phys. Chem. Lett.* **11**, 5115–5119 (2020).
20. Yang, S. et al. Stabilizing halide perovskite surfaces for solar cell operation with wide-bandgap lead oxysalts. *Science* **365**, 473–478 (2019).
21. Jiang, Q. et al. Surface passivation of perovskite film for efficient solar cells. *Nat. Photon.* **13**, 460–466 (2019).
22. Chen, H. et al. Quantum-size-tuned heterostructures enable efficient and stable inverted perovskite solar cells. *Nat. Photon.* **16**, 352–358 (2022).
23. Aber, A. G., Glunz, S. & Warta, W. Field effect passivation of high efficiency silicon solar cells. *Sol. Energy Mater. Sol. Cells* **29**, 175–182 (1993).
24. Jang, Y. W. et al. Intact 2D/3D halide junction perovskite solar cells via solid-phase in-plane growth. *Nat. Energy* **6**, 63–71 (2021).
25. Wu, W. Q. et al. Bilateral alkylamine for suppressing charge recombination and improving stability in blade-coated perovskite solar cells. *Sci. Adv.* **5**, eaav8925 (2019).
26. Kapil, G. et al. Tin-lead perovskite fabricated via ethylenediamine interlayer guides to the solar cell efficiency of 21.74%. *Adv. Energy Mater.* **11**, 2101069 (2021).
27. Hu, S. et al. Optimized carrier extraction at interfaces for 23.6% efficient tin–lead perovskite solar cells. *Energy Environ. Sci.* **15**, 2096–2107 (2022).
28. Frohna, K. et al. Nanoscale chemical heterogeneity dominates the optoelectronic response of alloyed perovskite solar cells. *Nat. Nanotechnol.* **17**, 190–196 (2021).
29. Baldo, M. A. & Forrest, S. R. Interface-limited injection in amorphous organic semiconductors. *Phys. Rev. B* **64**, 085201 (2001).

30. Saidaminov, M. I. et al. Multi-cation perovskites prevent carrier reflection from grain surfaces. *Nat. Mater.* **19**, 412–418 (2020).
31. Li, Z. et al. Organometallic-functionalized interfaces for highly efficient inverted perovskite solar cells. *Science* **376**, 416–420 (2022).
32. Zhang, F. et al. Metastable Dion-Jacobson 2D structure enables efficient and stable perovskite solar cells. *Science* **375**, 71–76 (2022).
33. Zhang, L. et al. Surface defect passivation of pb–sn-alloyed perovskite film by 1,3-propanediammonium iodide toward high-performance photovoltaic devices. *Sol. RRL* **5**, 2100299 (2021).
34. Zhang, F. et al. Surface lattice engineering through three-dimensional lead iodide perovskitoid for high-performance perovskite solar cells. *Chem* **7**, 774–785 (2021).
35. Park, B. et al. Understanding how excess lead iodide precursor improves halide perovskite solar cell performance. *Nat. Commun.* **9**, 3301 (2018).
36. Yan, N. et al. Ligand-anchoring-induced oriented crystal growth for high-efficiency lead-tin perovskite solar cells. *Adv. Funct. Mater.* **32**, 2201384 (2022).
37. Chiara, R. et al. The templating effect of diammonium cations on the structural and optical properties of lead bromide perovskites: a guide to design broad light emitters. *J. Mater. Chem. C Mater.* **10**, 12367 (2022).
38. Eperon, G. E. et al. Formamidinium lead trihalide: a broadly tunable perovskite for efficient planar heterojunction solar cells. *Energy Environ. Sci.* **7**, 982–988 (2014).
39. Zheng, X. et al. Defect passivation in hybrid perovskite solar cells using quaternary ammonium halide anions and cations. *Nat. Energy* **2**, 17102 (2017).
40. Stolterfoht, M. et al. How to quantify the efficiency potential of neat perovskite films: perovskite semiconductors with an implied efficiency exceeding 28%. *Adv. Mater.* **32**, 2000080 (2020).
41. Tong, J. et al. Carrier lifetimes of >1 ms in Sn-Pb perovskites enable efficient all-perovskite tandem solar cells. *Science* **364**, 475–479 (2019).
42. Lin, R. et al. Monolithic all-perovskite tandem solar cells with 24.8% efficiency exploiting comproportionation to suppress Sn(ii) oxidation in precursor ink. *Nat. Energy* **4**, 864–873 (2019).
43. Xiao, K. et al. All-perovskite tandem solar cells with 24.2% certified efficiency and area over 1 cm^2 using surface-anchoring zwitterionic antioxidant. *Nat. Energy* **5**, 870–880 (2020).
44. Wen, J. et al. Steric engineering enables efficient and photostable wide-bandgap perovskites for all-perovskite tandem solar cells. *Adv. Mater.* **34**, 2110356 (2022).
45. Song, T., Freidman, D. J. & Kopidakis, N. How useful are conventional I–Vs for performance calibration of single- and two-junction perovskite solar cells? A statistical analysis of performance data on ≈200 cells from 30 global sources. *Sol. RRL* **6**, 2100867 (2022).

Methods

Materials

All materials were used as received without further purification. Commercial ITO substrates (20 Ω per square, 25 × 25 mm^2) were purchased from TFD, Inc. Organic halide salts (FAI, FABr, MAI, BAI) and 4-fluorophenethylammonium bromide (4F-PEABr) were purchased from GreatCell Solar Materials. PEDOT:PSS aqueous solution (no. Al 4083) was purchased from Heraeus Clevios). PbI_2 (99.99%), $PbBr_2$ (99.999%), CsBr (over 99.0%) and Me-4PACz were purchased from TCI Chemicals. CsI (99.999%), SnI_2 (99.99%), SnF_2 (99%), glycine hydrochloride (99%), guanidine thiocyanate (GuaSCN, 99%) and ethane-1,2-diammonium iodide ($EDAI_2$, 98%) were purchased from Sigma-Aldrich. C_{60}, bathocuproine (BCP) and $PDAI_2$ were purchased from Xi'an Polymer Light Technology. All solvents used in the process were anhydrous and purchased from Sigma-Aldrich.

Perovskite precursor solutions

WBG perovskite. Wide-bandgap perovskite precursor solution (1.2 M, $FA_{0.8}Cs_{0.2}Pb(I_{0.6}Br_{0.4})_3$) was prepared by dissolving CsI, FAI, $PbBr_2$ and PbI_2 in a mixture of solvents DMF and DMSO at a volume ratio of 4:1. The precursor solution was stirred at 60 °C for 1 h and then filtered using a 0.22 μm polytetrafluoroethylene membrane before use.

NBG perovskite. Narrow-bandgap perovskite precursor solution (1.8 M, $Cs_{0.05}FA_{0.7}MA_{0.25}Pb_{0.5}Sn_{0.5}I_3$) was prepared by dissolving CsI, FAI, MAI, SnI_2 and PbI_2 in a mixture of DMF and DMSO at a volume ratio of 3:1. Tin powder (5 mg), GuaSCN (4 mg), SnF_2 (14 mg), 4F-PEABr (2 mg) and glycine hydrochloride (4 mg) were added to the precursor solution, which was then stirred at room temperature for 1 h. The precursor solution was filtered using a 0.22 μm polytetrafluoroethylene membrane before use.

Solar cell fabrication

Single junction wide bandgap perovskite solar cells. NiO_x nanocrystal (10 mg ml^{-1} in H_2O and 2-Propanol mixed solvent with volume ratio of 3:1) layers were first spin-coated on ITO substrates at 3,000 rpm for 25 s in air without any post-treatment, then the substrates were immediately transferred to the glovebox. The NiO_x nanoparticles were prepared via the hydrolysis reaction of nickel nitrate referring to our previous work[46]. Me-4PACz (0.3 mg ml^{-1}) in ethanol was spin-coated on the NiO_x film at 3,000 rpm for 25 s and then annealed at 100 °C for 10 min. For the perovskite film fabrication, the substrate was spun at 4,000 rpm for 32 s with an acceleration of 1,000 rpm, 100 μL Anisole was dropped onto the substrate during the last 8 s of the spinning. The substrates were then transferred onto a hotplate and heated at 100 °C for 15 min. The organic salts surface treatment solutions were prepared by dissolving $PDAI_2$, and BAI in IPA with different concentrations. The optimal concentration of $PDAI_2$ used in devices was 1 mg ml^{-1}. The surface treatment was finished by depositing 130 μl organic salts solution onto the perovskite film surface at a spin rate of 4,000 rpm for 25 seconds with a 1,000 rpm s^{-1} acceleration. The film was then annealed at 100 °C for 5 min. After cooling down to room temperature, the substrates were transferred to the evaporation system and a 20-nm-thick C_{60} film was subsequently deposited on top by thermal evaporation at a rate of 0.2 A s^{-1}. The substrates were then transferred to the atomic layer deposition (ALD) system (Picosun) to deposit 20 nm SnO_2 at 90 °C using precursors of tetrakis(dimethylamino) tin (iv) (99.9999%) and deionized water. A 140 nm Ag electrode was then deposited by thermal evaporation.

Single-junction Pb–Sn perovskite solar cells. Prepatterned ITO glass substrates were sequentially cleaned using acetone and isopropanol. PEDOT:PSS was spin-coated on ITO substrates at 6,000 rpm for 30 s and annealed on a hot plate at 160 °C for 20 min in ambient air. After cooling we transferred the substrates immediately to a nitrogen-filled glovebox for deposition of perovskite films, which were deposited with a two-step spin-coating procedure: (1) 1,000 rpm for 10 s at acceleration 200 rpm s^{-1} and (2) 3,800 rpm for 45 s at acceleration 1,000 rpm s^{-1}; 300 μl of chlorobenzene was dropped onto the spinning substrate during the second spin-coating step at 20 s before the end of the procedure. Substrates were then treated on the hot plate for 10 min at 100 °C. Post treatment with $EDAI_2$ was carried out by spin-coating a solution of 0.5 mg ml^{-1} $EDAI_2$ in 4:3 isopropyl alcohol (IPA)IPA:toluene at 4,000 rpm for 25 s, followed by annealing at 100 °C for 5 min. Next, 20 nm of C60, 8 nm of BCP and 140 nm of Ag were sequentially deposited on top of the perovskite layer by thermal evaporation[46].

All-perovskite tandem solar cells. Wide-bandgap perovskite solar cell fabrication was completed as described above until deposition of ALD SnO_2, after which 1 nm of Au was deposited by thermal evaporation. Next, PEDOT:PSS (diluted at a 1:2 volume ratio in IPA) was spin-coated onto the WBG subcell at 4,000 rpm for 30 s and annealed at 120 °C for 10 min. Substrates were then cooled and transferred to a N_2-filled glovebox for deposition of the NBG subcell. The NBG perovskite precursor solution was spin-coated onto substrates at 1,000 rpm for 10 s, followed by 3,800 rpm for 45 s. At 20 s before the end of the second step, 300 μl of chlorobenzene was dropped onto the substrate, which was then annealed at 100 °C for 10 min. Post treatment with EDA was carried out by spin-coating a solution of 0.5 mg ml^{-1} $EDAI_2$ in 4:3 IPA:toluene at 4,000 rpm for 25 s, followed by annealing at 100 °C for 5 min. Finally, C_{60} (30 nm), ALD SnO_2 (20 nm) and Ag (140 nm) were sequentially deposited as described above.

Device testing

Current density–voltage (*J–V*) characteristics were measured using a Keithley 2400 source meter under illumination from a solar simulator (Newport, Class A) with a light intensity of 100 S5 mW cm^{-2} (checked with a calibrated reference solar cell from Newport). *J–V* curves were measured in a nitrogen atmosphere with a scanning rate of 100 mV s^{-1} (voltage step of 10 mV and delay time of 200 ms). The active area was determined by the aperture shade mask (0.049 cm^2 for small-area devices) placed in front of the solar cell. A spectral mismatch factor of 1.0 was used for all *J–V* measurements. For stabilized output measurements at MPP, the device testing chamber was maintained under ambient conditions. Solar cells were fixed at the MPP voltage (determined from *J–V* sweeps in both scanning directions) and current output was tracked over time. EQE measurements were performed in ambient air using a QuantX-300 Quantum Efficiency Measurement System (Newport), with monochromatic light focused on the device pixel and a chopper frequency of 20 Hz. For tandem solar cells, EQE measurements were performed in ambient air and bias illumination from bright LEDs, with emission peaks of 850 and 450 nm used for measurement of the front and back subcells, respectively. No bias voltage was applied during EQE measurement of tandem solar cells.

Stability testing

Devices were placed in a homemade stability-tracking station. For single-junction devices, the illumination source was a white light LED with intensity calibrated to match 1 sun conditions. For tandem solar cells, an AM1.5G solar simulator illumination source (G2V sunbrick) with an intensity of 100 mW cm^{-2} was used. For room temperature tests (ISOS-L-1I), the device chamber was sealed and supplied with continuous N_2 purging. MPPs were tracked by a perturb-and-observe algorithm that updates the MPP point every 10 s. Encapsulation was performed using a capping device with a glass slide, with ultraviolet-adhesive (Lumtec LT-U001) as sealant.

GIWAXS

GIWAXS measurements were conducted at the BXDS (LE-wiggler) beamline of the Canadian Light Source (CLS) using X-rays of wavelength

λ = 0.82 Å, at a grazing incidence angle of either 0.15° or 1.00° and an exposure time of 5 s. Grazing incidence X-ray diffraction patterns were collected by a MarCCD 225 detector with a sample–detector distance of 430 mm, and are presented in q-coordinates using the equation $q = 4\pi\sin\theta\,\lambda^{-1}$, where θ is half of the diffraction angle. In the present grazing incidence X-ray diffraction data, q was calibrated by measurement of XRD from a Lanthanum hexaboride reference sample. Images were calibrated using LaB6 and processed via the Nika software package[47] and GIXSGUI MATLAB plug-in[48].

Drift-diffusion simulations

Simulations of perovskite solar cells were conducted in the heterojunction solar cell simulator SCAPS-1D, v.3.3.07 (ref. [49]).

Transient-absorption/time-resolved spectroscopy

Femtosecond laser pulses of 1,030 nm generated by a Yb:KGW laser at 5 kHz repetition rate (Pharos (Light Conversion)) were passed through an optical parametric amplifier (Orpheus (Light Conversion)) selected for 450 nm light. The beam passed through the parametric amplifier served as the pump pulse, whereas the probe pulse was generated by focusing the initial 1,030 nm pulse into a sapphire crystal, which resulted in a white light continuum (Helios (Ultrafast)). With a temporal resolution of the system of around 250 fs, each time step meant delaying the probe pulse with respect to the pump, with time steps that increased exponentially. Every other pump pulse was blocked with a chopper to determine the change in optical density. After passing through a grating spectrograph, pulses were measured by means of a charge-coupled device (Helios (Ultrafast)).

Intensity-dependent PLQY measurements

The excitation source was an unfocused beam of a 442 nm continuous-wave diode laser. Photoluminescence was collected using an integrating sphere with a precalibrated fibre coupled to a spectrometer (Ocean Optics QE Pro) with an intensity of approximately 300 mW cm^{-2}. PLQY values were calculated by $\mathrm{PLQY} = \frac{P_S}{P_{Ex} \times A}$, where $A = 1 - \frac{P_L}{P_{Ex}}$ represents absorption, P_S is the integrated photon count of sample emission following laser excitation, P_{Ex} is the integrated photon count of the excitation laser when the sample is removed from the integrating sphere and P_L is the integrated photon count of the excitation laser when the sample is mounted in the integrating sphere and hit by the beam. A set of neutral-density filters were used to vary excitation density.

Time-resolved photoluminescence spectroscopy

Time-resolved photoluminescence measurements were performed using a Horiba Fluorolog time-correlated single-photon counting system with photomultiplier tube detectors. A pulsed laser diode (532 nm, 110–140 ps pulse width) was used as excitation source for steady-state and transient measurements. For transient measurements, a 160 ns period (0.28 nJ per pulse) was used to capture accurate carrier lifetimes.

IPES and UPS

For combined UPS and IPES measurements, an Excitech H Lyman-α photon source (10.2 eV) with an oxygen-filled beam path was used for excitation, coupled to a PHI 5600 ultrahigh vacuum system with a hemispherical electron energy analyser. A sample bias of −5 V and pass energy of 5.85 eV were used for UPS acquisition. IPES measurements were performed in Bremsstrahlung isochromat mode with electron kinetic energy below 5 eV and an emission current of 2 μA to minimize sample damage. A Kimball Physics ELG-2 electron gun with a BaO cathode was used to generate the electron beam, and emitted photons were collected with a bandpass photon detector that included an optical bandpass filter (280 nm for 3-fluoro-phenethylammonium (3F-PEA) and BA-treated films and 254 nm for control and phenethylammonium (PEA)-treated films) and a photomultiplier tube (R585, Hamamatsu Photonics). Samples were held at a −20 V bias during all IPES measurements and the UHV chamber was blacked out to exclude external light.

Perovskite films sent for combined UPS/IPES were fabricated on ITO/NiO_x/Me-4PACz substrates.

Transient photovoltage and photocurrent

These measurements were carried out according to ref. [50].

KPFM

Kelvin probe force microscopy (KPFM) images were generated using an Asylum Cypher S atomic force microscope (Oxford Instruments) with a Ti-Ir-coated ASYELEC.01-R2 cantilever and $k = 4 \pm 0.5$ N m^{-1} (Asylum Research). Scans were performed over 2 μm at 512 pixels and 0.5 Hz in a two-pass nap method, the first pass in tapping mode and the second in KPFM mode with a tip potential of 5 V and surface clearance of 5 nm. Cantilever calibration was performed using the Asylum Research GetReal database.

Hyperspectral imaging

Perovskite films were deposited on HTL/ITO films using the same method as for device fabrication, and the C_{60} film was evaporated on top of the perovskite films to deliver a *pin* device stack. Absolute PL spectra of encapsulated samples were collected using a hyperspectral imaging system coupled to a microscope with 2 nm spectral resolution (Photon etc. IMA). Samples were excited from the top surface of perovskite (and C_{60} layer) with a 405 nm laser at around 1 sun illumination[51]. The absolute calibration procedure of the setup is reported in detail elsewhere[52]. The collected data were analysed by home-built MatLab code using modified Würfel's generalized Plank law to acquire QFLS, $\Delta\mu$ (refs. [53–56]):

$$\varphi_{(E,\theta)} = A_{(E,\theta)} \frac{\cos\theta}{4\pi^3\hbar^3 c_0^2} E^2 \frac{1}{\exp\left(\frac{E-\Delta\mu}{k_B T}\right) - 1}$$

where $A_{(E,\theta)}$ is the absorption probability of a photon with energy E, incident at angle θ with respect to the normal surface; $k_B T$ is the Boltzmann constant and temperature (equivalent to 25.7 meV at room temperature). Here, the $\cos\theta$ factor represents emission from the surface following Lambert's law. Finally, fitting is applied to each data cube to construct the images with two-pixel averaging, giving a spatial resolution of about 0.6 μm per pixel.

SEM

High-resolution SEM images were obtained using a Hitachi S5200 microscope with an accelerating voltage of 1.5 kV. A low accelerating voltage and low beam current were deployed to reduce surface damage of perovskite films under electron beam bombardment.

Pseudo-*J*–*V* curves

Pseudo-*J*–*V* curves were plotted based on intensity-dependent PLQY measurements. First, QFLS is calculated based on PLQY values at various excitation light intensities:

$$\mathrm{QFLS} = k_B T \times \ln(\mathrm{PLQY} \times S \times J_G / J_{0,\mathrm{rad}})$$

where S is sun-equivalent excitation intensity, J_G the current density generated at 1 sun (taken from device J_{SC}) and $J_{0,\mathrm{rad}}$ the radiative recombination current in the dark (taken from the dark current value from Shockley–Queisser limit).

Because the current density generated is proportional to excitation light intensity, an exponential current–QFLS curve is created that ideally follows the same functional dependence on voltage as the dark current–voltage curve of a diode with no series resistance. Subtracting this from a charge generation current density at 1 sun (J_G) creates a *pJ*–*V*

curve that is limited by nonradiative recombination processes in the cell, but not by transport and/or series resistance.

DFT calculations

All density functional theory (DFT) calculations were done using FHI-aims code[57–59]. Default numerical settings, referred to as 'intermediate' in FHI-aims, were used. Local minimum-energy geometries of Born–Oppenheimer surfaces were obtained with residual total energy gradients below 1×10^{-2} eV Å^{-1} for atomic positions, by the PBE–generalized gradient approximation functional[60] within the Van der Waals corrections, followed by the Tkatcheko–Scheffler (TS)[61] method. DOS is calculated by the PBE–generalized gradient approximation functional, including spin-orbit coupling effects[62], within a k-point grid of $2 \times 2 \times 1$ to sample the Brillouin zone corresponding to the unit cell shown in Supplementary Fig. 7b,c.

To mimic the experimental composition $Cs_{0.2}FA_{0.8}Pb(I_{0.6}Br_{0.4})_3$, an alloyed structure was first built using a $2 \times 2 \times 2$ supercell based on cubic phase conventional cells (Supplementary Fig. 7a) within $Cs_{0.25}FA_{0.75}Pb(I_{0.584}Br_{0.416})_3$. Next, the slab structures (Supplementary Fig. 7b,c) with total *c* axis set to 100 Å were built based on these PBE + TS relaxed alloyed structures in a $1 \times 1 \times 3$ supercell for Pb-I-terminated and (FA, Cs)-I-terminated surfaces. Detailed surface configurations are very important for prediction of work function tunability, which will be largely affected by surface terminations and defects. As a result, three different surface configurations (perfect surface, surface with one iodine vacancy (V_I) and surface with one bromine vacancy (V_{Br})) are considered for Pb-I terminations. On the other hand, five different surface configurations (perfect surface, surface with one Cs vacancy (V_{Cs}), surface with one FA vacancy (V_{FA}), surface with one iodine vacancy (V_I) and surface with one bromine vacancy (V_{Br})) are considered for (FA, Cs)-I terminations. In all geometry relaxations for the slab, the bottom three layers of atoms are fixed to mimic the bulk environment and the atomic positions of all atoms besides these three layers are relaxed by PBE + TS.

Based on these relaxed slab structures, we can calculate the work function changes resulting from PDA treatment according to the electrostatic potential difference between the treated surface (ligands on top; Supplementary Fig. 8b (bottom)) and untreated surface (Supplementary Fig. 8b (top)), as shown in Supplementary Fig. 8c. Among different surface configurations (Supplementary Fig. 8a), the Pb-I-terminated surface with V_{Br} provides the closest agreement for ΔW after PDA treatment (theoretically calculated value, 0.44 eV) with the experimental UPS data (experimental result, 0.1 eV; Fig. 1c). Next, detailed DOS comparison is used to elucidate potential changes to surface states after PDA treatment and their corresponding n-/p-doping effects. In DOS comparison plots, the contribution from the third-bottom fixed Pb-I layers in the slab (Supplementary Fig. 7c) is used to align DOS positions to the bulk case (Supplementary Fig. 9).

Reporting summary

Further information on research design is available in the Nature Portfolio Reporting Summary linked to this article.

Data availability

All data are available in the main text or supplementary materials. The data that support the findings of this study are available from the corresponding authors on reasonable request.

Code availability

The code that supports the findings of this study is available from the corresponding authors on reasonable request.

46. Chen, H. et al. Efficient and stable inverted perovskite solar cells incorporating secondary amines. *Adv. Mater.* **31**, 1903559 (2019).
47. Ilavsky, J. Nika: software for two-dimensional data reduction. *J. Appl. Crystallogr.* **45**, 324–328 (2012).
48. Jiang, Z. GIXSGUI: a MATLAB toolbox for grazing-incidence X-ray scattering data visualization and reduction, and indexing of buried three-dimensional periodic nanostructured films. *J. Appl. Crystallogr.* **48**, 917–926 (2015).
49. Burgelman, M., Nollet, P. & Degrave, S. Modelling polycrystalline semiconductor solar cells. *Thin Solid Films* **361–362**, 527–532 (2000).
50. Shao, Y., Yuan, Y. & Huang, J. Correlation of energy disorder and open-circuit voltage in hybrid perovskite solar cells. *Nat. Energy* **1**, 15001 (2016).
51. Aydin, E. et al. Ligand-bridged charge extraction and enhanced quantum efficiency enable efficient n–i–p perovskite/silicon tandem solar cells. *Energy Environ. Sci.* **14**, 4377–4390 (2021).
52. Delamarre, A., Lombez, L. & Guillemoles, J. F. Characterization of solar cells using electroluminescence and photoluminescence hyperspectral images. *J. Photonics Energy* **2**, 027004 (2012).
53. Rau, U. Reciprocity relation between photovoltaic quantum efficiency and electroluminescent emission of solar cells. *Phys. Rev. B Condens. Matter Mater. Phys.* **76**, 085303 (2007).
54. Wurfel, P. The chemical potential of radiation. *J. Phys. C Solid State Phys.* **15**, 3967–3985 (1982).
55. El-Hajje, G. et al. Quantification of spatial inhomogeneity in perovskite solar cells by hyperspectral luminescence imaging. *Energy Environ. Sci.* **9**, 2286–2294 (2016).
56. Wurfel, P., Finkbeiner, S. & Daub, E. Generalized Planck's radiation law for luminescence via indirect transitions. *Appl. Phys. A* **60**, 67–70 (1995).
57. Ren, X. et al. Resolution-of-identity approach to Hartree–Fock, hybrid density functionals, RPA, MP2 and GW with numeric atom-centered orbital basis functions. *New J. Phys.* **14**, 053020 (2012).
58. Havu, V., Blum, V., Havu, P. & Scheffler, M. Efficient O(N) integration for all-electron electronic structure calculation using numeric basis functions. *J. Comput. Phys.* **228**, 8367–8379 (2009).
59. Blum, V. et al. Ab initio molecular simulations with numeric atom-centered orbitals. *Comput. Phys. Commun.* **180**, 2175–2196 (2009).
60. Perdew, J. P., Burke, K. & Ernzerhof, M. Generalized gradient approximation made simple. *Phys. Rev. Lett* **77**, 3865–3868 (1996).
61. Tkatchenko, A. & Scheffler, M. Accurate molecular van der Waals interactions from ground-state electron density and free-atom reference data. *Phys. Rev. Lett.* **102**, 073005 (2009).
62. Huhn, W. P. & Blum, V. One-hundred-three compound band-structure benchmark of post-self-consistent spin-orbit coupling treatments in density functional theory. *Phys. Rev. Mater.* **1**, 033803 (2017).

Acknowledgements We thank J. Warby for a useful discussion that contributed to our understanding of perovskite–ETL interfaces, and T. Song and N. Kopidakis at NREL for device certification. Z.W. acknowledges the Banting Postdoctoral Fellowships Program of Canada. GIWAXS patterns were collected at the BXDS-WLE Beamline at CLS with the assistance of C.-Y. Kim and A. Leontowich. This research was made possible by the US Department of the Navy, Office of Naval Research (grant nos. N00014-20-1-2572 and N00014-20-1-2725) and the US Department of Energy's Office of Energy Efficiency and Renewable Energy under Solar Energy Technologies Office Award no. DE-EE0008753. This work was supported in part by the Ontario Research Fund Research Excellence programme (ORF7: Ministry of Research and Innovation, Ontario Research Fund-Research Excellence Round 7). This work was also supported by the King Abdullah University of Science and Technology under award no. OSR-CRG2020-4350. This work was authored in part by the National Renewable Energy Laboratory, operated by Alliance for Sustainable Energy for the US Department of Energy under contract no. DE-AC36-08GO28308. NREL authors acknowledge support from the Operational Energy Capability Improvement Fund of the Department of Defense. The views expressed in the article do not necessarily represent the views of the Department of Energy or the US Government. CLS is funded by NSERC, the Canadian Institutes of Health Research, CFI, the Government of Saskatchewan, Western Economic Diversification Canada and the University of Saskatchewan. This work was also supported by the Natural Sciences and Engineering Council of Canada and the Vanier Canada Graduate Scholarship.

Author contributions H.C., A.M., S.T. and B.C. planned experiments and coordinated the work. H.C. fabricated WBG devices and tandems for performance and certification and fabricated perovskite films for characterization. H.C., A.M., C. Li and L.C. fabricated NBG devices and tandems. S.T. and A.M. wrote the original draft. S.T., B.C., E.U. and S.D.W. carried out optical spectroscopy of films and devices and performed data analysis. T.Z. carried out DFT calculations. G.H. and S.D.W. performed UPS measurements and data analysis. P.S. and T.F. carried out KPFM and data analysis. S.T. and L.G. performed GIWAXS measurements and analysed data. J.W., Z.W., L.Z., S.M.P. and L.G. helped optimize the single-junction and tandem device structure. R.A.A. conducted thermal admittance spectroscopy measurements. X.Z., J.M.L., C.X., B.S., C. Liu, Y. Yang, M.G.K. and N.J.P. assisted with device analysis and data interpretation. E.H.S., Y. Yan, S.D.W. and M.G.K. secured funding and helped to review and edit the manuscript.

Competing interests The authors declare no competing interests.

Additional information

Supplementary information The online version contains supplementary material available at https://doi.org/10.1038/s41586-022-05541-z.

Correspondence and requests for materials should be addressed to Yanfa Yan or Edward H. Sargent.

Peer review information *Nature* thanks Weijun Ke and the other, anonymous, reviewer(s) for their contribution to the peer review of this work. Peer reviewer reports are available.

nature research

Corresponding author(s): Edward Sargent
Yanfa Yan

Solar Cells Reporting Summary

Nature Research wishes to improve the reproducibility of the work that we publish. This form is intended for publication with all accepted papers reporting the characterization of photovoltaic devices and provides structure for consistency and transparency in reporting. Some list items might not apply to an individual manuscript, but all fields must be completed for clarity.

For further information on Nature Research policies, including our data availability policy, see Authors & Referees.

Experimental design

Please check: are the following details reported in the manuscript?

1. Dimensions

Area of the tested solar cells	☒ Yes ☐ No	Device testing in Methods
Method used to determine the device area	☒ Yes ☐ No	Device testing in Methods

2. Current-voltage characterization

Current density-voltage (J-V) plots in both forward and backward direction	☒ Yes ☐ No	Figure 3a & 4d
Voltage scan conditions *For instance: scan direction, speed, dwell times*	☒ Yes ☐ No	Figure 3a,b & 4d,e
Test environment *For instance: characterization temperature, in air or in glove box*	☒ Yes ☐ No	Device testing in Methods
Protocol for preconditioning of the device before its characterization	☒ Yes ☐ No	Solar cell fabrication and device testing in Methods
Stability of the J-V characteristic *Verified with time evolution of the maximum power point or with the photocurrent at maximum power point; see ref. 7 for details.*	☒ Yes ☐ No	Stability testing in Methods, Figure 3b & Figure 4e

3. Hysteresis or any other unusual behaviour

Description of the unusual behaviour observed during the characterization	☐ Yes ☒ No	Negligible hysteresis
Related experimental data	☒ Yes ☐ No	Throughout main text and supplementary information

4. Efficiency

External quantum efficiency (EQE) or incident photons to current efficiency (IPCE)	☒ Yes ☐ No	Figure 4c, Figure S15
A comparison between the integrated response under the standard reference spectrum and the response measure under the simulator	☒ Yes ☐ No	Certified results in Fig. 3b, Fig. 4e, supplementary figs. 16, 23
For tandem solar cells, the bias illumination and bias voltage used for each subcell	☒ Yes ☐ No	Device testing in methods

5. Calibration

Light source and reference cell or sensor used for the characterization	☒ Yes ☐ No	Device testing in methods
Confirmation that the reference cell was calibrated and certified	☒ Yes ☐ No	Device testing in methods

Calculation of spectral mismatch between the reference cell and the devices under test	☒ Yes ☐ No	Device testing in methods

6. Mask/aperture

Size of the mask/aperture used during testing	☒ Yes ☐ No	Device testing in methods
Variation of the measured short-circuit current density with the mask/aperture area	☒ Yes ☐ No	Figure S16, S17, S23, S24

7. Performance certification

Identity of the independent certification laboratory that confirmed the photovoltaic performance	☒ Yes ☐ No	Main text, Figure 3b & 4e, Fig. S16, S23
A copy of any certificate(s) *Provide in Supplementary Information*	☒ Yes ☐ No	Fig S16, S23

8. Statistics

Number of solar cells tested	☒ Yes ☐ No	Fig 3c
Statistical analysis of the device performance	☒ Yes ☐ No	Fig 3c

9. Long-term stability analysis

Type of analysis, bias conditions and environmental conditions *For instance: illumination type, temperature, atmosphere humidity, encapsulation method, preconditioning temperature*	☒ Yes ☐ No	Fig 4f, stability testing in methods